Hindawi Publishing Corporation
Journal of Nanomaterials
Volume 2016, Article ID 6034790, 12 pages
http://dx.doi.org/10.1155/2016/6034790

Research Article

Microstructure and Mechanical Properties of Mg/2 wt.%SiC_p Nanocomposite Fabricated by ARB Process

Zheng Lv, Xueping Ren, Wenjing Wang, Xiaodan Gao, and Wenjie Li

School of Materials Science and Engineering, University of Science and Technology Beijing, Beijing 100083, China

Correspondence should be addressed to Zheng Lv; lvzheng1988@126.com

Received 5 May 2016; Revised 31 August 2016; Accepted 8 September 2016

Academic Editor: Domenico Acierno

Magnesium matrix nanocomposites (MMNC, the same below) containing 2 wt.% nanosized SiC_p were fabricated through accumulative roll bonding (ARB). The microstructure and mechanical properties of Mg/2 wt.%SiC_p nanocomposites are reported for various ARB cycles. To evaluate microstructure of the nanocomposites, the field emission scanning electron microscope (FE-SEM), X-ray diffractometer (XRD), and transmission electron microscope (TEM) were applied. After fourteen ARB cycles, the nanocomposite showed a homogeneous distribution of reinforcements and a significant reduction in average matrix grain size. Meanwhile, the nanocomposite revealed a higher percentage of recrystallization and lower intensity of basal texture as compared to monolithic Mg. Mechanical properties were investigated through tensile and microhardness tests. The strength and elastic modulus and microhardness of Mg/2 wt.%SiC_p were found to be improved significantly from eight ARB cycles and reach maximum values at fourteen ARB cycles. The ultimate tensile strength, yield strength, microhardness, and elastic modulus of Mg/2 wt.%SiC_p are considerably increased by 17.6%, 61.0%, 72.7%, and 80.8% as compared to raw Mg, respectively.

1. Introduction

Magnesium matrix composites have been extensively applied in many fields, such as aerospace and light metal automotive applications, due to their low density and superior specific properties including strength, stiffness, and creep resistance [1–10]. The necessity of reducing environmental pollution and protecting natural resources also gives rise to the development of magnesium-based composites with superior mechanical properties [2]. It is widely recognized that judicious selection of type, size, and fraction of reinforcements assists in realizing enhanced dimensional stability, damping capacity, and elevated temperature properties [3]. An observable improvement in both mechanical and other desirable properties can be attributed to the conjoint and interactive influence of the properties of the matrix and reinforcement phase, coupled with the size, shape, orientation, volume fraction, and distribution of reinforcement phase in magnesium matrix [4].

In the past, various types of reinforcements have been used in magnesium matrix to synthesize composites possessing higher strength, while the silicon carbide (SiC) remains the most commonly selected reinforcement phase. It has been reported that the presence of micron-sized SiC_p led to an increase in hardness and modulus of Mg matrix while reducing the ultimate tensile strength [3, 4]. In recent years, lots of literature proved that the use of nanosized reinforcements promises to affect both ultimate tensile strength and yield strength of Mg matrix favorably [1, 2, 5–10]. Ferkel and Mordike [5] manufactured the MMNC containing 3 vol.%SiC_p (30 nm) by powder metallurgy. Cao et al. [1, 6] reported that the nano-SiC_p reinforced MMNC fabricated by ultrasonic cavitation both enhanced the UTS and YS of the matrix. Nie et al. [7] synthesized the MMNC containing 1.0 vol.%SiC_p (60 nm) via ultrasonic vibration and obtained a significant improvement in UTS and YS. Thakur [2] fabricated the 1% SiC_p (50 nm) reinforced MMNC by microwave assisted powder metallurgy, with the increase in UTS by 7.78% and YS by 9.84%, respectively.

To produce magnesium matrix composites, a number of conventional processes have been introduced that can broadly be categorized in two processes, namely, powder metallurgy (PM, such as microwave assisted PM route [2, 5]) and ingot metallurgy techniques (IM, such as stirring casting,

squeeze casting, ultrasonic vibration or cavitation [1, 6, 7], and disintegrated melt deposition [3, 8, 9]). As the most established severe plastic deformation for the production of sheet metals, accumulative roll bonding (ARB) processes have been utilized for the synthesis of metal matrix composites in recent years [11–19]. The repeated stacking and rolling process offer the possibility of producing materials with tailored properties by producing sandwich-like laminates or introducing phases like particles or films [11]. In nanocomposites produced by ARB, well dispersion of nanoparticles could, in theory, be always achieved in the case of sufficient ARB cycles. Furthermore, conventional synthesis process and hot working process of MMNC could be integrated through ARB process. ARB processes have been successfully utilized to produce aluminum matrix composites [12–16] or nanocomposites [11, 17, 18]. Yoo et al. [19] have published the report on AZ31-0.06 vol.% CNT nanocomposites fabricated by 4-cycle ARB process. But, till date, no report is available on the Mg-SiC_p nanocomposites produced by ARB process.

The present work focuses on the Mg/SiC_p nanocomposites produced by ARB process. The objective of the study is to manufacture finely dispersed Mg/2 wt.%SiC_p nanocomposites with superior mechanical properties by ARB process. A novel method for incorporation of nanosized reinforcements was adopted by ultrasonic-assisted liquid phase deposition, and hot pack rolling was applied in each ARB cycle. The microstructure evolution and mechanical properties of the produced nanocomposites are investigated.

2. Experimental Procedure

2.1. Materials. The annealed sheets of industrial pure magnesium (>99.5%) with a dimension of 125 × 55 × 1 mm were used as rolled samples. Analytical grade of SiC powder with an average size of 50 nm was used as reinforcement (Figure 1). The raw Mg sheets had an average grain size of 14.7 μm, as shown in Figure 2. The ultimate tensile strength (UTS), yield strength (YS), elastic modulus (E), and microhardness of raw Mg sheet are 247.4 MPa, 155.9 MPa, 35.9 GPa, and 46.6 HV, respectively.

2.2. Preparation. Before ARB, the surfaces of Mg sheets were cleaned and degreased. These sheets were scratch brushed with the stainless steel brush and then degreased in acetone. For first ARB cycle, six layers of raw Mg sheets were stacked, and SiC nanoparticles were dispersed on one side of each of the inner four sheets. In present work, the incorporation of SiC nanoparticles was achieved by employing stabilized particle suspended liquids and applying these from the liquid phase to the metal surface through ultrasonic-assisted liquid phase deposition. Each deposition process was the same and was restricted to one sheet. The block copolymer Disperbyk-2150 (BYK Chemie GmbH) was first dissolved in ethanol, and then the weighed SiC nanoparticles were added to the as-prepared solution. The block copolymer Disperbyk-2150 is a good dispersing agent to improve the dispersion of nanoparticles in ethanol and stabilize the suspension of the nanoparticles. This mixture was put into an ultrasonic bath and ultrasonicated for 30 min at least. After adding Mg

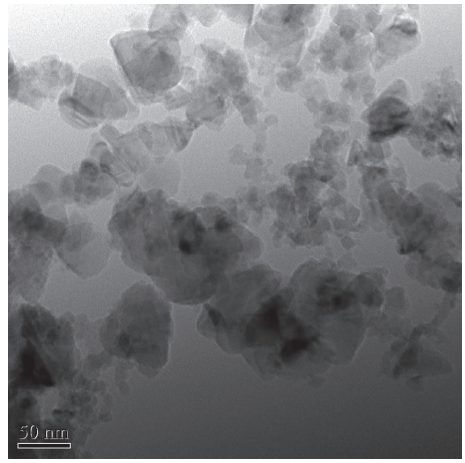

Figure 1: TEM micrograpy of SiC nanoparticles used in this work.

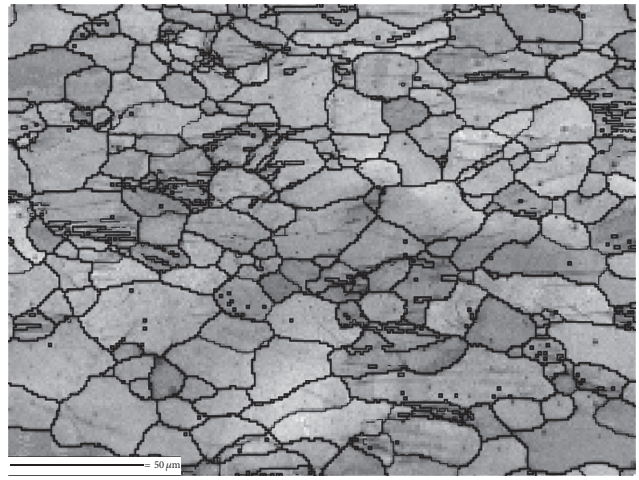

Figure 2: EBSD grain boundary map of the raw magnesium sheet. RD-ND section with RD parallel to scale bar.

sheet, the suspended liquid was further ultrasonicated until the ethanol was evaporated. Six layers of Mg sheets were stacked together and then were assembled with the self-designed rolling pack. In order to prevent the reaction or bonding between Mg sheets and pack, the outside of each of the outer two Mg sheets was applied to antisolder flux. The schematic diagram of a self-designed rolling pack is presented in Figure 3. The rolling pack is comprised of four 6061 aluminum alloy plates with dimensions of 160 × 96 × 1 mm and 160 × 20 × 6 mm. The pack is rigidly fixed with blind rivets at the front end and fastened with steel wire at the tail end. There are six holes for riveting at front end and two holes for fastening at tail end.

2.3. ARB Process. The roll bonding process was carried out with no lubrication, using a two-high experimental rolling mill provided by the Engineering Research Institute of USTB (University of Science and Technology Beijing). The rolls were designed with 350 mm diameter and 550 mm barrel length. The as-prepared material was heated to 673 K for

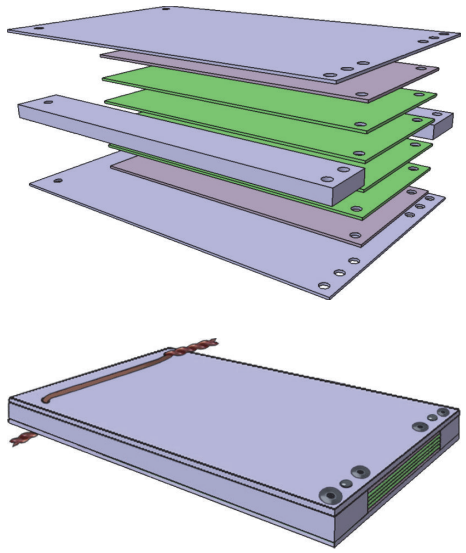

Figure 3: The schematic diagram of self-designed rolling pack for ARB process.

30 min and then subjected to a series of rolling with 50% reduction and the speed of 1 m/min. After rolling, the pack was manually disassembled. This cycle was named one ARB cycle. Subsequently, the nanocomposite sheet was cut into two halves, scratch brushed, degreased in acetone, and stacked over each other, without incorporation of nanoparticles between them. The rolling pack and antisolder flux were employed in each ARB cycle. The cyclic ARB process was carried out for up to 14 cycles. To compare the microstructural evolution and mechanical properties, monolithic Mg was also prepared with the same process.

2.4. Characterization. The RD-ND planes (RD denotes rolling direction and ND denotes direction normal to plate surface) of nanocomposites were metallographically ground and polished to observe the interfacial bonding condition and how well the nanoparticles were distributed. ZEISS ULTRA 55 field emission scanning electron microscopy (SEM) was used for above observations. Prior to EBSD (Electron Backscattered Diffraction) measurements, the RD-ND planes were ground by standard emery from 2000 to 3000 grades and then electrolytic polished in a 10% $HClO_4$ ethanol solution. The concrete parameters of electrolytically polishing are as follows: applied voltage ~15 V, current density ~0.12 A/cm^2, temperature ~−30°C, and duration 120–150 s. The FE-SEM equipped with an HKL EBSD system was used to collect microstructure information in selected three areas (subsurface, quarter thickness, and center). The EBSD results were handled through Channel 5 software. All microscale measurements were conducted using Image-Pro Plus 6.0 software. The overall texture was evaluated by X-ray diffraction (XRD) using a Philips X'pert MRD. Incomplete pole figures of $\{0\ 0\ 0\ 2\}$, $\{1\ 0\ -1\ 0\}$, $\{1\ 0\ -1\ 1\}$, $\{1\ 0\ -1\ 2\}$, and $\{1\ 1\ -2\ 0\}$ were recorded, and the ODF (Orientation Distribution Functions) was constructed using Textool software. Recalculated pole figures of $\{0\ 0\ 0\ 2\}$ and $\{1\ 0\ -1\ 0\}$ and inverse pole figures in RD direction were then derived from the ODFs. Tensile tests were carried out for the sheets with various ARB cycles at a nominal strain rate of 1.0×10^{-3} s^{-1} at ambient temperature by using a servohydraulic universal testing machine (CMT4105, China). The dimension of tensile test specimen is shown in Figure 4. Micro Vickers hardness measurement was performed by using LEICA VMHT 30 M digital microhardness tester attached with a Vickers indenter. The measurement was carried out through thickness at a test load of 25 gf for a dwell time of 15 s, and the average microhardness of each specimen was calculated and recorded.

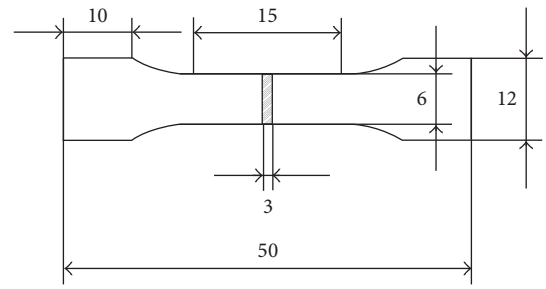

Figure 4: Schematic drawing of tensile specimen (mm).

3. Results and Discussion

3.1. Microstructures. Figure 5 shows the SEM micrograph of the interfaces of Mg/2 wt.%SiC_p nanocomposites produced by the ARB process in 4 and 14 cycles. It can be seen that after four cycles, there are many big agglomerated and clustered nanoparticles in Mg matrix. The length of clusters reached ~50 μm in ND and ~180 μm in RD. As the ARB process continued, the length of clusters decreased. Vaidyanath et al. [20] proposed the film theory (i.e., the rapture of surface oxide layers) to be a major mechanism in the roll bonding process for pure metals. In present work, after surface preparation, the raw Mg sheets were immediately immersed in the suspended liquid and then covered with SiC nanoparticles layers during the deposition process. Thus, during rolling the nanoparticles layers break up coherently to expose the underlying metals which are extruded under normal roll pressure. Therefore, the interface was a combination of nanoparticles clusters and bonded areas of extruded magnesium after four cycles. As the ARB cycle increased, the clusters tended to be elongated along RD direction and even some were further fragmented into smaller pieces (microclusters). After fourteen ARB cycles, the clusters almost disappeared. Although the nanocomposite contains 6×2^{13} magnesium layers and 5×2^{13} nanoparticles layers in theory after fourteen ARB cycles, the interfaces can not be identified at low magnification. In other words, SiC nanoparticles dispersed from the interfaces to magnesium matrix after fourteen ARB cycles. The SEM micrograph at high magnification further demonstrates the homogeneous distribution of nanoparticles in matrix. Actually, after fourteen ARB cycles, the average distance of bond layers (i.e., thickness of individual magnesium layer, ~60 nm) approximately equals to average size of SiC_p (50 nm). Thus, a homogeneous distribution of nano-SiC_p can be obtained

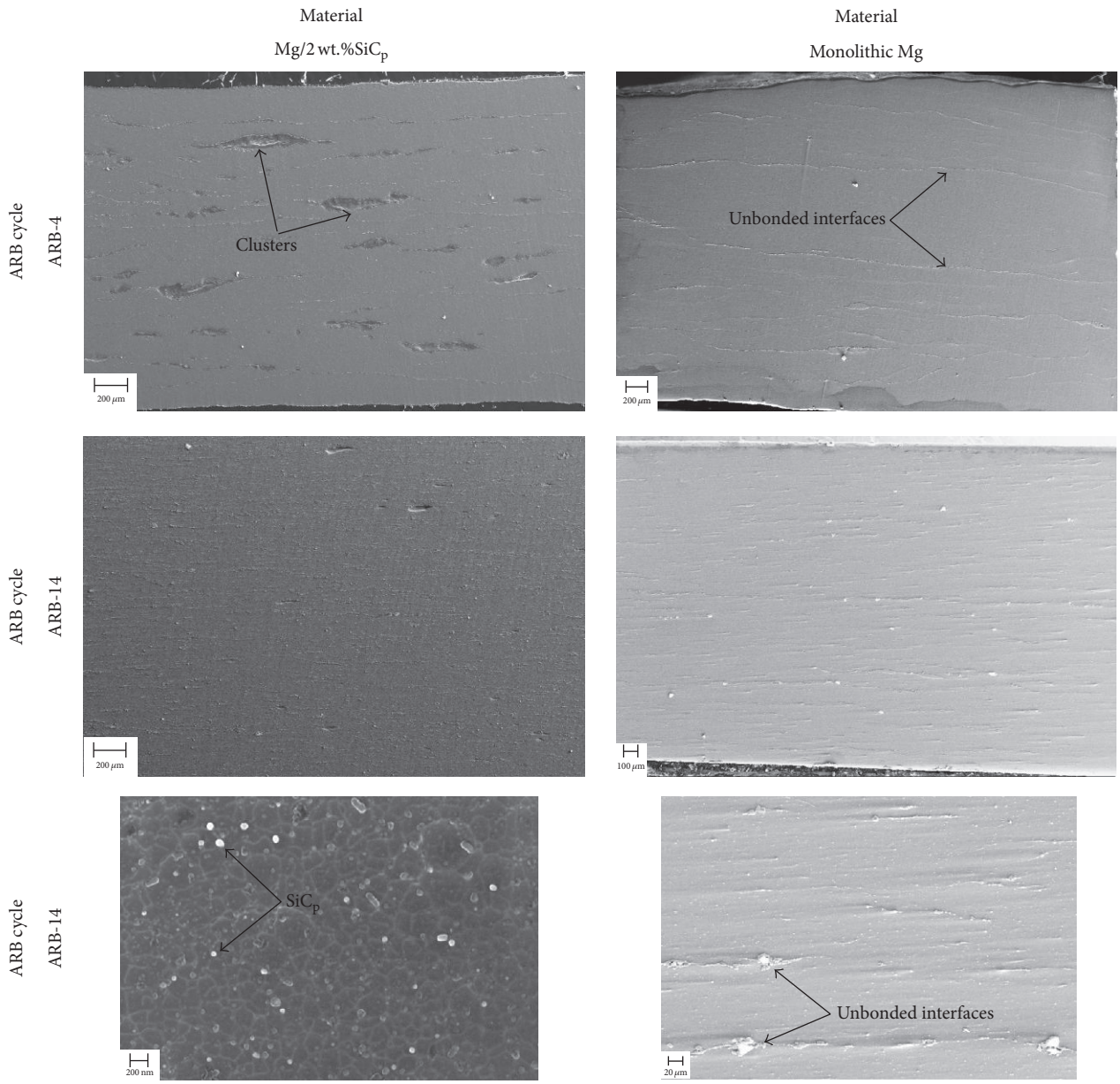

Figure 5: SEM micrographs of the Mg/2 wt.%SiC_p produced by four ARB cycles and fourteen ARB cycles.

theoretically after fourteen ARB cycles. Figure 6 shows a typical TEM image of the interface between components in Mg/2 wt.%SiC_p. The interface is clean and generally free of reaction productions. SiC_p bonds well with Mg matrix.

For the purpose of comparing the bonding interfaces, the SEM micrographs of the interfaces of monolithic Mg produced by the ARB process were also shown in Figure 5. However, after 14 ARB cycles, the bonding interfaces of monolithic Mg sample are more obvious as compared to Mg/2 wt.%SiC_p. Thus, the bonding could not be soundly formed without the assistance of the nano-SiC_p. The oxide layer formed during heat preservation at 673 K (30 min) would deteriorate the bonding between adjacent Mg sheets. In present work, there is no time lag between wire-brushing and nanoparticle deposition; more importantly, the nano-SiC_p layers could prevent oxidation of Mg sheets to an extent during the heat preservation. Therefore, the interfaces of Mg/2 wt.%SiC_p were bonded more effectively than monolithic Mg.

As shown in Figure 7, EBSD is applied to analyze the microstructure of Mg/2 wt.%SiC_p and monolithic Mg in various ARB cycles (4, 8, 11, and 14). The blue, yellow, and red grains are denoted as recrystallized, substructured, and deformed grains, respectively. The EBSD measurements were done throughout the thickness of the sheets, and the maps at three different thickness locations (i.e., subsurface, quarter thickness, and center) are shown for each material. Average grain size at three thickness locations in Mg/2 wt.%SiC_p and monolithic Mg are illustrated in Table 1 for various

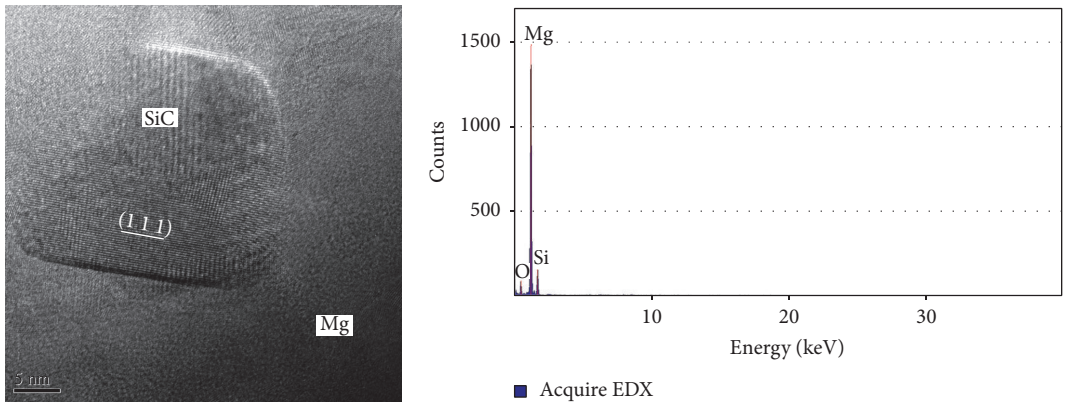

(a) (b)

Figure 6: HRTEM image and EDX pattern of the interface between nano-SiC_p and Mg in nanocomposite.

Table 1: Average grain size (μm) at three thickness locations in the Mg/2 wt.%SiC_p and monolithic Mg sheets for various ARB cycles.

ARB cycles	Mg/2 wt.%SiC_p							Monolithic Mg						
	2	3	4	6	8	11	14	2	3	4	6	8	11	14
Subsurface	5.3	6.9	4.0	6.9	3.1	3.2	3.0	4.5	1.5	5.6	4.7	3.2	3.0	6.4
1/4 thickness	7.2	13.1	7.4	8.3	4.6	6.9	3.6	5.6	3.8	7.2	6.0	4.9	3.9	4.7
Center	7.0	15.2	6.9	15.5	4.2	7.2	2.9	4.9	1.7	16.7	5.5	4.3	2.7	6.9
Total	6.5	11.7	6.1	10.2	3.9	5.8	3.2	5.0	2.3	10.0	5.4	4.1	3.2	6.0

ARB cycles. For nanocomposite, the calculation of grain sizes related to Mg matrix only, and the nanosized SiC particles were excluded from the calculation. From Figure 7 and Table 1, it can be observed that the grain size distribution is generally uneven for both two materials. The grain size at surface is relatively finer and evener than that at quarter thickness and center. It is well known that under high friction conditions, for example, hot rolling, the metals deform inhomogeneously through thickness because a large amount of redundant shear strain is introduced in the surface regions [21]. For Mg/2 wt.%SiC_p especially, the presence of nanoparticle layers or clusters could hinder the transferring of strain from surface to inner, because of which there are bulk coarse grains at quarter thickness and center. On the other hand, the additional local strain around individual nano-SiC_p could lead to local grain refinement [11]. Thus, the uneven microstructure at quarter thickness and center can be attributed to the inhomogeneous deformation through thickness and the presence of nanoparticle layers/clusters for Mg/2 wt.%SiC_p. However, after 14 ARB cycles, the microstructure is quite even and fine at each location. It indicates that the difference in the grain size distribution owing to redundant shear strain and SiC_p clusters is homogenized by repeating the ARB cycle [22]. The average grain size of Mg/2 wt.%SiC_p reached a minimum (3.2 μm) after 14 ARB cycles.

Figure 8 shows the grain boundaries misorientation distribution and recrystallized fraction of the monolithic Mg and Mg/2 wt.%SiC_p produced by 14-cycle ARB process. Compared with monolithic Mg, Mg/2 wt.%SiC_p had a higher proportion of recrystallized grains (~48% in average) and high angle grain boundaries. It indicates that the SiC nanoparticles contribute to grain refinement by stimulating the dynamic recrystallization (DRX) nucleation. That is, of course, based on the homogeneous distribution of SiC nanoparticles (14 ARB cycles). Furthermore, the addition of SiC nanoparticles led to inhibiting the grain growth through potential pinning effect. For both materials, the misorientation distribution plots show a strong peak in low angle boundary regime (<15°) and a small peak at around 30°. Notably, for Mg/2 wt.%SiC_p, there is a small fraction of high angle boundaries ($86^\circ \leq \theta \leq 90^\circ$) in the misorientation distribution, which corresponds to the $\{1\ 0\ -1\ 2\}$ twinning (i.e., $86^\circ\ \langle 1\ 1\ -2\ 0\rangle \pm 5^\circ$) during the ARB process.

The development of texture of monolithic Mg and Mg/2 wt.%SiC_p at various ARB cycles is presented in pole figures (Figure 9) and inverse pole figures (Figure 10). The texture type of monolithic Mg and Mg/2 wt.%SiC_p is basal-type, where the basal $\{0\ 0\ 0\ 2\}$ planes are parallel to the sheet surface (basal poles perpendicular to RD). For both materials, the intensity of $\{0\ 0\ 0\ 2\}$ texture was reduced with ARB cycles; the spread of $\{0\ 0\ 0\ 2\}$ orientations tended to change from transverse direction to rolling direction with ARB cycles. Generally, the intensity of basal texture increases with increasing strain. However, in present work, repeated preheating during ARB passes had an annealing effect on the materials and weakened the basal texture. Importantly, the addition of SiC nanoparticles reduced the intensity of basal component during ARB process. After fourteen ARB cycles, the pole intensity of $(0\ 0\ 0\ 2)$ pole figures was 15.5 and 12.8 for monolithic Mg and Mg/2 wt.%SiC_p, respectively. This is attributed to the recrystallization and nucleation of

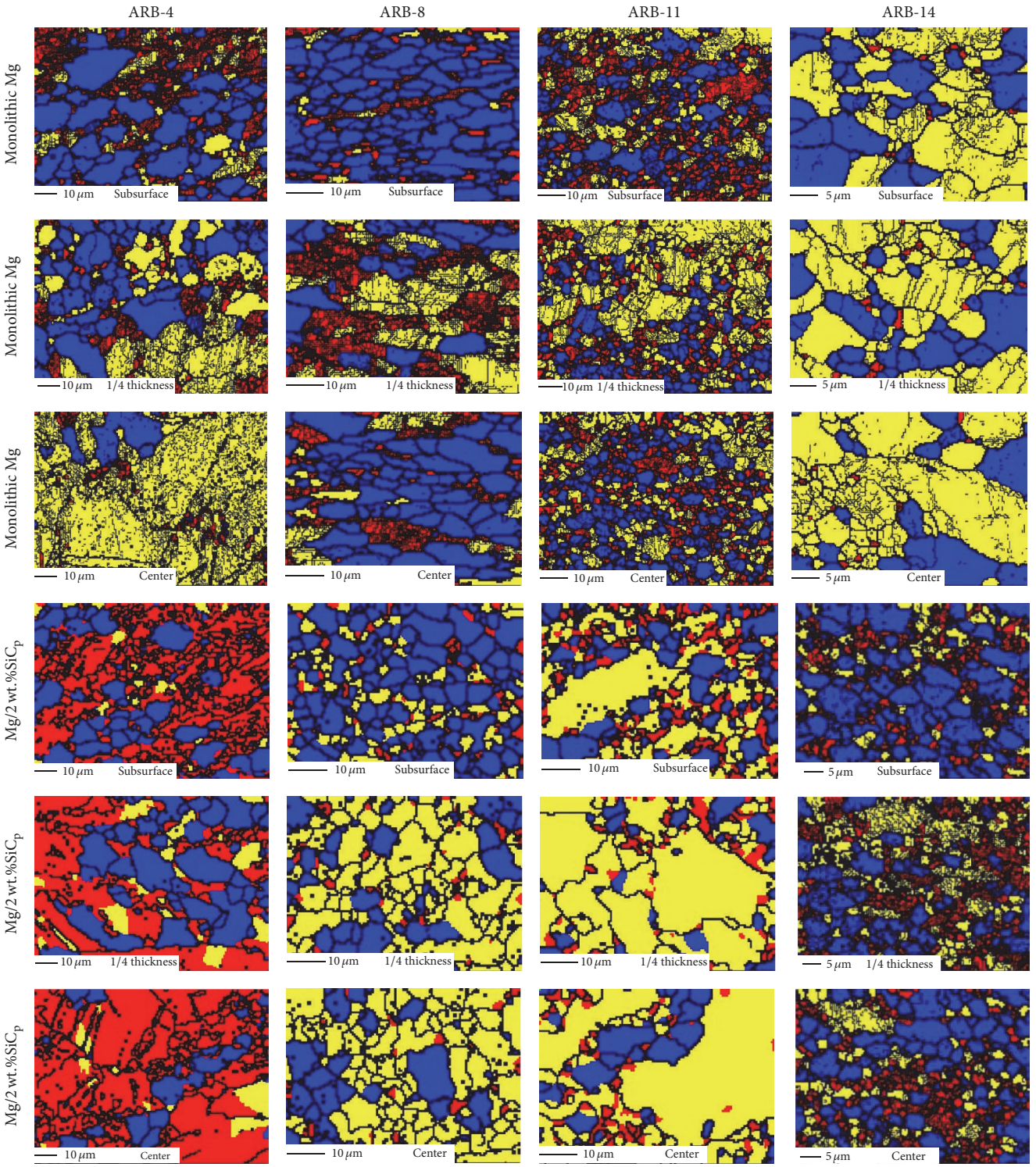

FIGURE 7: EBSD recrystallization maps of the monolithic Mg and Mg/2 wt.%SiC_p produced by ARB process in various cycles: four, eight, eleven, and fourteen cycles. The blue, yellow, and red grains are denoted as recrystallized, substructured, and deformed grains, respectively. RD-ND section with RD parallel to scale bar.

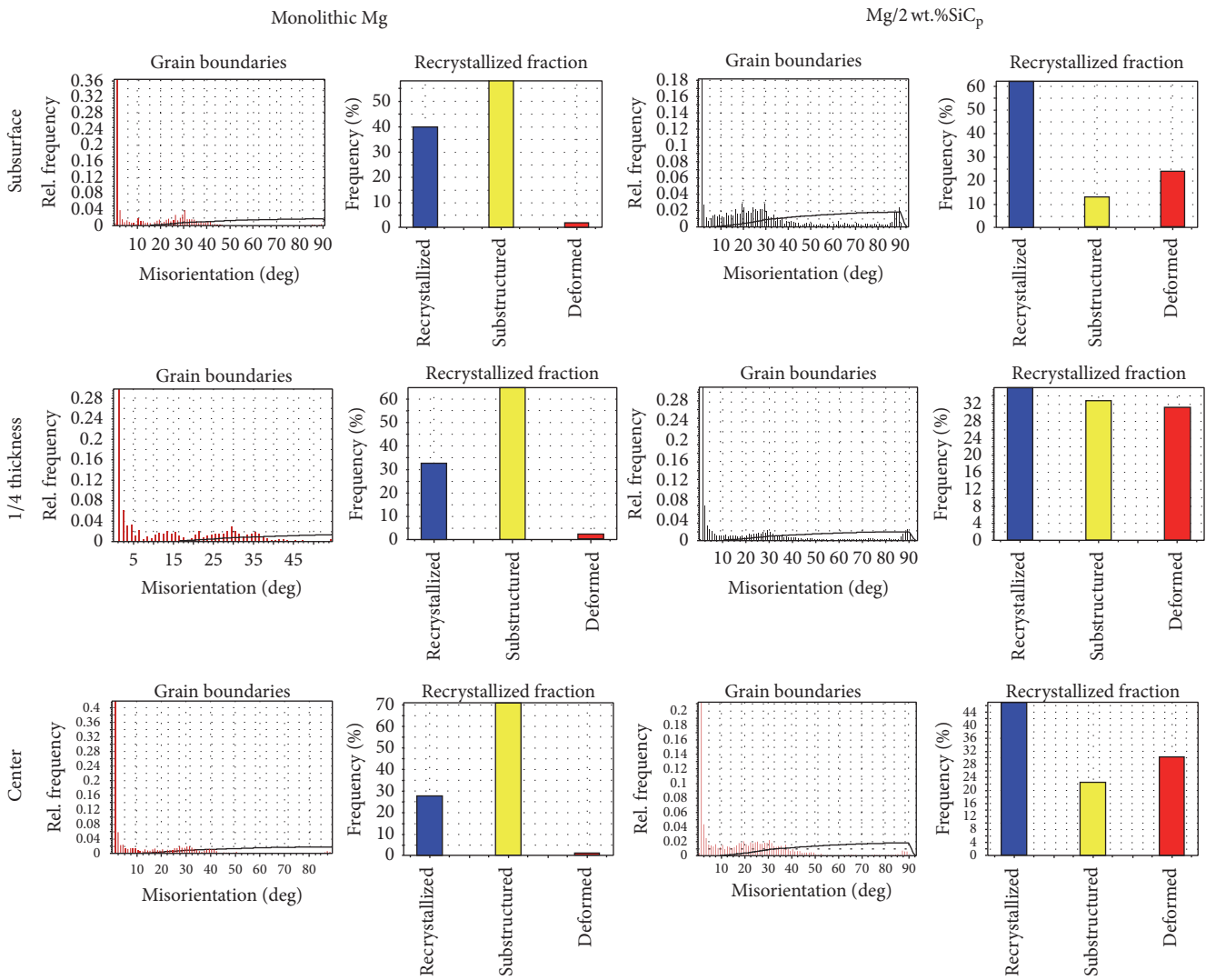

Figure 8: Grain boundaries misorientation distribution and recrystallized fraction of the monolithic Mg and Mg/2 wt.%SiC_p produced by 14-cycle ARB process.

new grains at orientation angles different from the parent grains. The results are also supported by the EBSD analysis (Figure 8).

The $\{0\ 0\ 0\ 2\}$ basal texture observed in the materials can be a deformation texture (due to rolling associated with ARB process) or a mixture texture (containing deformation texture and recrystallization texture) [23]. As shown in Figure 10, for monolithic Mg, the $(0\ 0\ 0\ 2)\ \langle 1\ 0\ -1\ 0\rangle$ deformation texture and $(0\ 0\ 0\ 2)\ \langle 1\ 1\ -2\ 0\rangle$ recrystallization texture are observed; for Mg/2 wt.%SiC_p, $(0\ 0\ 0\ 2)\ \langle 1\ 1\ -2\ 0\rangle$ recrystallization texture is observed due to the sufficient dynamic recrystallization after eight ARB cycles.

3.2. Mechanical Properties. The mechanical behaviors of the Mg/2 wt.%SiC_p and monolithic Mg for various ARB cycles were assessed in terms of their tensile properties and microhardness. The true stress-strain curves of the ARB processed Mg/2 wt.%SiC_p and monolithic Mg for various ARB cycles are shown in Figure 11. To compare tensile properties, UTS (ultimate tensile strength), YS (yield strength), and E (elastic modulus) of the Mg/2 wt.%SiC_p and monolithic Mg sheets are summarized in Table 2.

For Mg/2 wt.%SiC_p, UTS and YS were seriously weakened before six ARB cycles (compared to raw Mg). Obviously, the poor performance of Mg/2 wt.%SiC_p is mainly due to the presence of SiC_p clusters and coarse grains in Mg matrix. From Figure 11(a), the discontinuous plastic-segment under 2-cycle also demonstrates that the SiC_p clusters adversely affect the strength of nanocomposite. SiC_p clusters act as crack or decohesion nucleation sites at stresses lower than the matrix yield strength, causing the nanocomposites to fail at unpredictable low-stress levels. After eight ARB cycles, UTS and YS of Mg/2 wt.%SiC_p increase with the ARB cycles up to fourteen cycles. From Table 2, it is clear that the maximum value of tensile strength is obtained after the fourteenth ARB cycle (291.1 MPa in UTS and 251.1 MPa in YS which are 17.6% and 61.1% higher than those of raw magnesium). Several

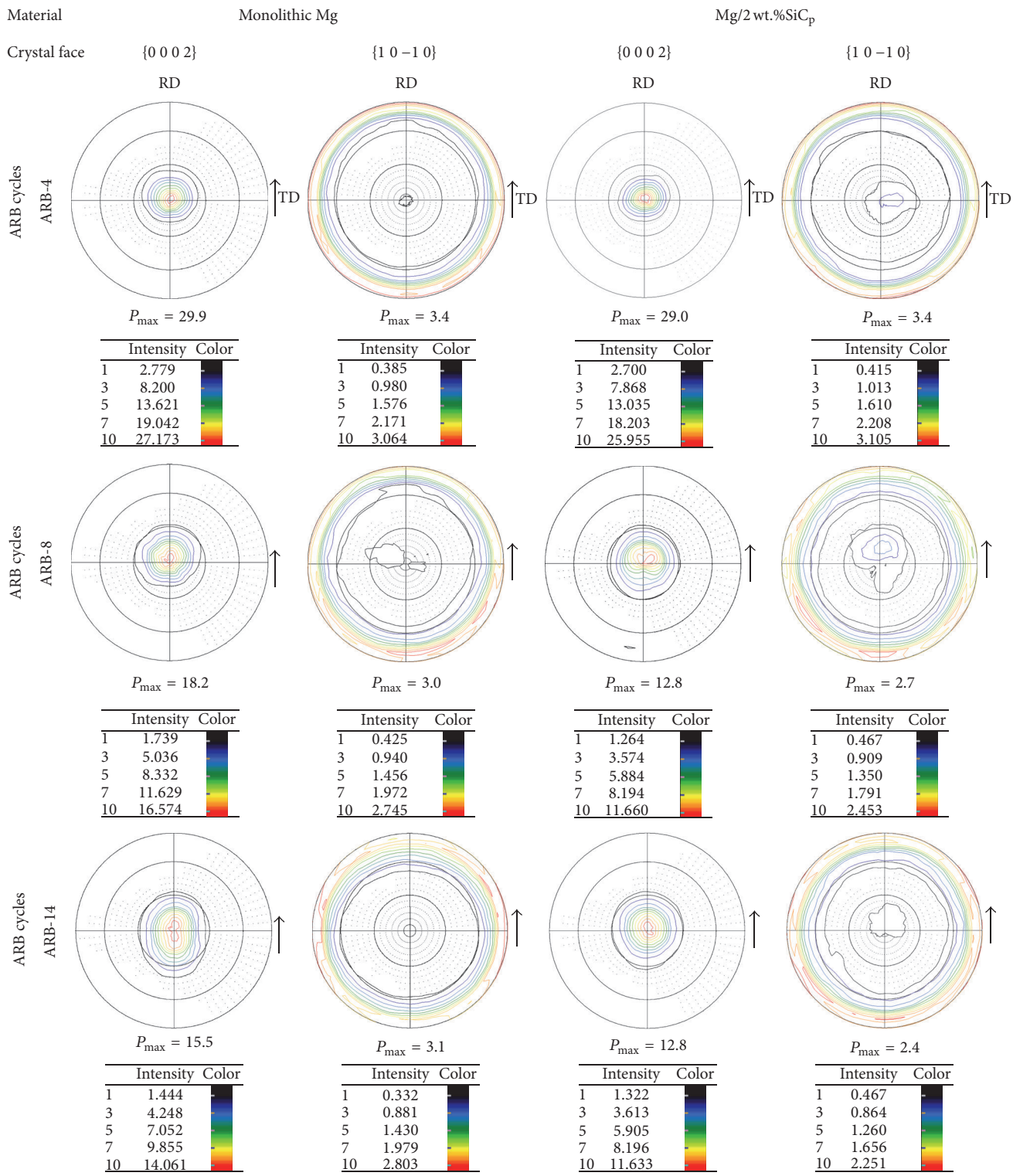

FIGURE 9: The texture of monolithic Mg and Mg/2 wt.%SiC_p produced by ARB process in various cycles: four, eight, and fourteen. The texture in the form of (0 0 0 2) and (1 0 −1 0) pole figures.

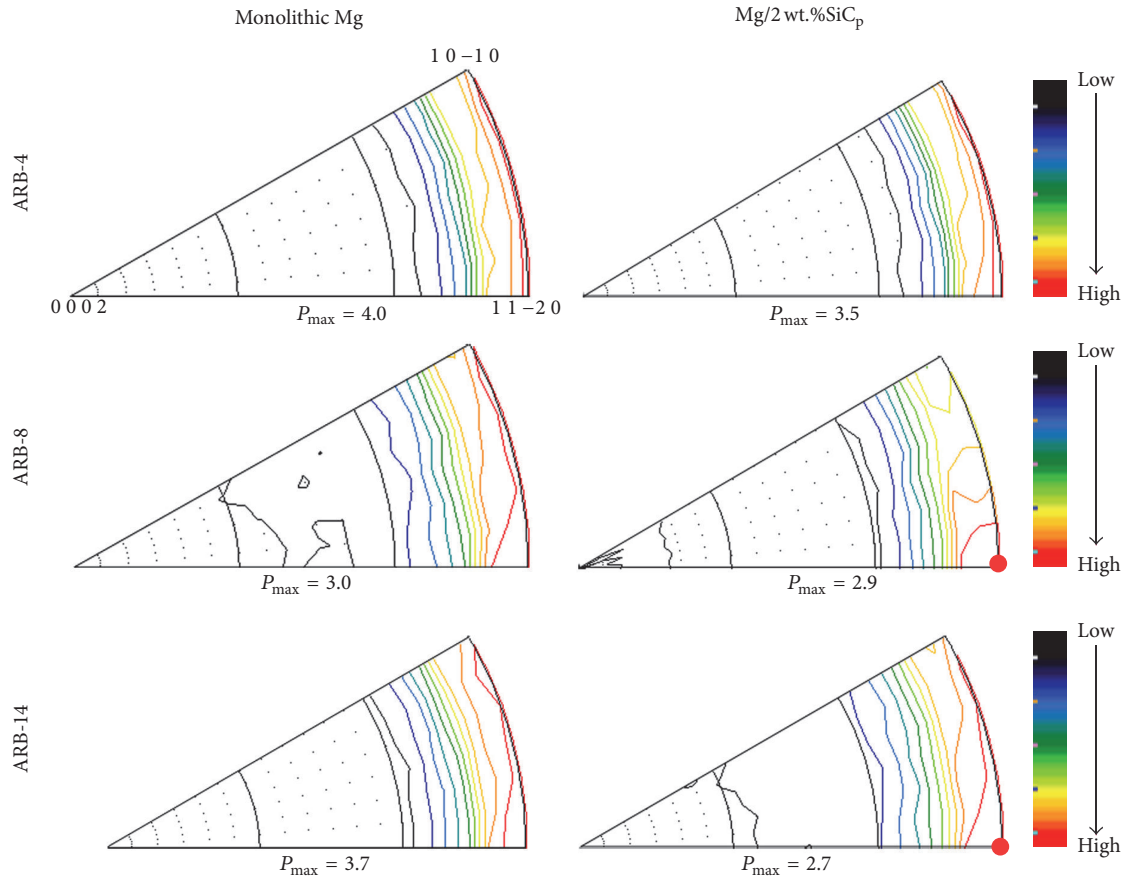

FIGURE 10: The inverse pole figures in RD direction for monolithic Mg and Mg/2 wt.%SiC_p produced by ARB process in various cycles: four, eight, and fourteen.

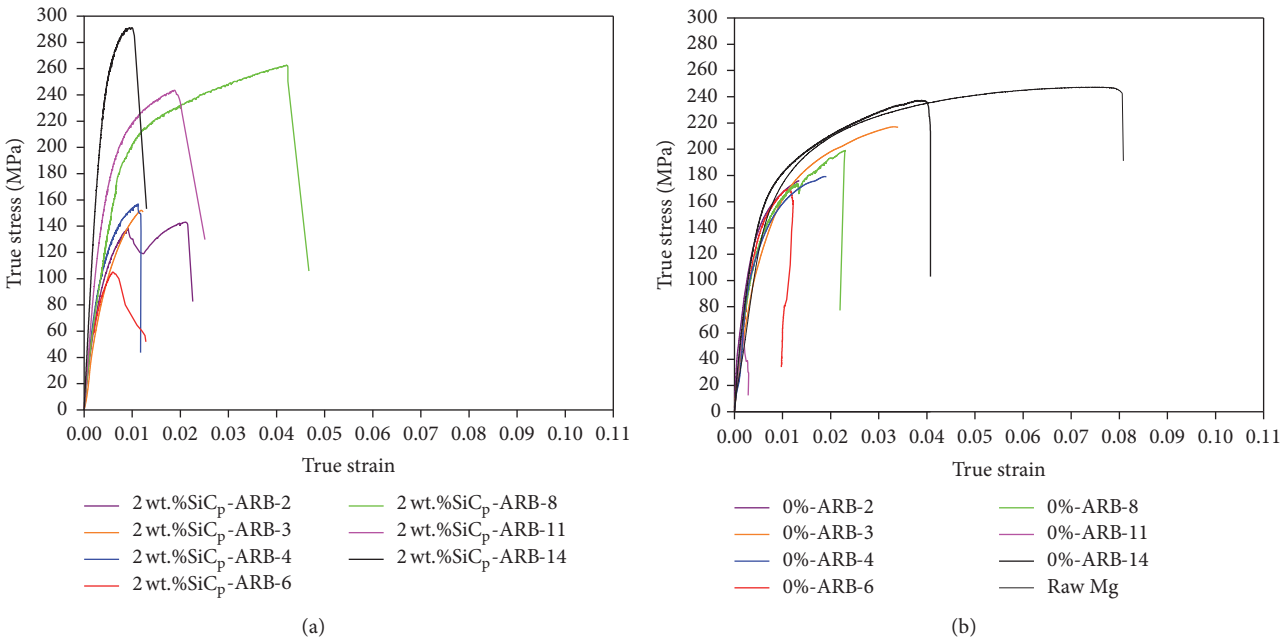

FIGURE 11: The true stress-strain curves of (a) Mg/2 wt.%SiC_p and (b) monolithic Mg produced by ARB process in various cycles.

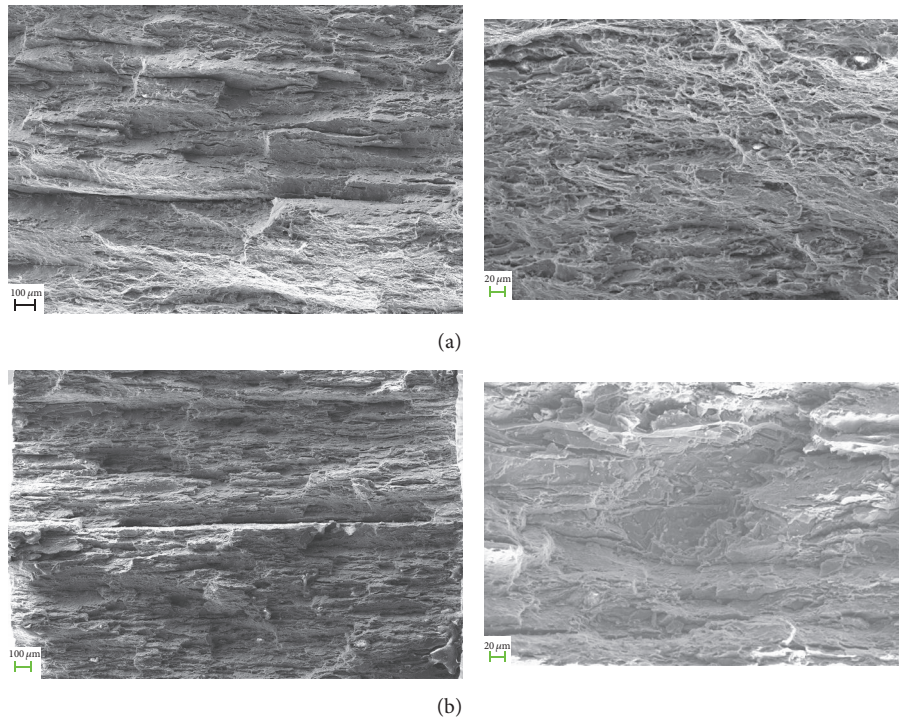

Figure 12: Fracture morphologies of (a) monolithic Mg and (b) Mg/2 wt.%SiC_p produced by 14-cycle ARB process.

Table 2: Tensile properties (UTS, 0.2YS%, and E) and microhardness of the Mg/2 wt.%SiC_p and monolithic Mg for various ARB cycles.

ARB cycles	UTS (MPa)		YS (MPa)		E (GPa)		Microhardness (HV)	
	MMNC	Mg	MMNC	Mg	MMNC	Mg	MMNC	Mg
2	143.0	176.0	109.5	145.0	25.5	43.7	47.1 ± 0.8	47.9 ± 1.2
3	152.1	217.1	120.2	142.4	33.2	27.2	48.5 ± 1.4	47.8 ± 1.2
4	157.0	179.2	118.5	119.9	37.8	32.1	49.9 ± 1.3	48.4 ± 1.6
6	105.0	170.1	93.5	146.7	37.2	33.0	47.9 ± 1.4	49.1 ± 0.9
8	243.6	199.1	183.8	128.9	31	30.9	68.1 ± 1.3	46.3 ± 1.0
11	262.7	60.4	189.9	49.0	45.9	37.8	73.4 ± 2.6	61.5 ± 1.5
14	291.2	237.5	250.1	130.1	64.9	21.4	80.5 ± 1.4	67.6 ± 1.2

works have reported that the strength variations in ARBed materials are governed by two main strengthening mechanism: grain refinement and strain hardening by dislocations [24, 25]. In present work, recrystallization of nanocomposites during hot rolling could weaken the effect of strain hardening. At higher cycles, grain refinement contributes to the higher strength as the ARB cycles increase. It is important that, in our work, strengthening of the nanocomposites does not only result from the above two mechanisms but that it is also affected by the uniformity of nanoparticles in matrix, reinforcing role of nanoparticles in matrix, and the condition of Mg/SiC interface. Firstly, the homogeneous distribution of nanoparticles (Figure 5) contributes to the higher strength at higher cycles by effectively pinning the dislocation motion in matrix. And second, the strain mismatch between matrix and reinforcement leads to a high density of dislocation around reinforcements, which increases the initial stress to operate the dislocations. At last, good interfacial adhesion between matrix and reinforcements (Figure 6) could result in efficient load transfer of the applied stress from the soft matrix to harder reinforcements.

In contrast, the monolithic Mg has a poor performance in tensile strength at all ARB cycles (compared to raw Mg). The reason perhaps is the weak interfacial bonding due to surface oxidation of raw Mg sheets. In Mg/2 wt.%SiC_p, the SiC_p layers could effectively hinder the surface oxidation of Mg sheets during the preheating; from SEM micrograph (Figure 5) there is no visible unbonded interface found after fourteen ARB cycles. However, for monolithic Mg, the bare surfaces of Mg sheets are extremely easy to be oxidized during preheating (Figure 5). It is obviously that the presence of high-temperature oxide layers adversely affects the interfacial bonding, which would further deteriorate the tensile strength.

E values of Mg/2 wt.%SiC_p and monolithic Mg have been evaluated through true stress-strain curves (Figure 11). The

E values of Mg/2 wt.%SiC_p and monolithic Mg at various ARB cycles are illustrated in Table 2. It is clearly that the elastic modulus of Mg/2 wt.%SiC_p processed by fourteen ARB cycles was significantly improved (64.5 GPa) compared to raw Mg (35.9 GPa). In contrast, E value of monolithic Mg has no improvement through ARB process. Generally, elastic modulus is an intrinsic property for a single phase material. In case of composites, when the reinforcements are uniformly distributed in matrix, the rule of mixture (ROM) can provide a fair approximation of the overall elastic modulus of the composites material. Lahiri et al. [26] have reported that there is a good match between the computed and experimentally obtained E values for Al-2 vol.% CNTs composites. In present work, the relatively lower E values of nanocomposites prior to eight ARB cycles are mainly ascribed to the nanoparticle clusters in matrix. Elastic modulus for magnesium (35.9 GPa) and SiC_p (~250 GPa) is very different; thus, during loading process the plastic deformation starts at SiC_p depleted regions. As a result, the effective elastic modulus is much lower for the nanocomposites containing inhomogeneously distributed nanoparticles [26]. After fourteen ARB cycles, however, the experimental E value not only has significantly increased by 80.8% compared to raw magnesium but also is far beyond the computed E (~38.3 GPa) value using ROM (Rule of Mixture). Further attempts are needed to explore the reinforcing role of SiC nanoparticle in Mg matrix.

The fracture surfaces of two materials subjected to fourteen ARB cycles are shown in Figure 12. The figures reveal that monolithic Mg exhibits an obvious delamination fracture (in low magnification), having a gray fibrous appearance with hemispheroidal dimples (in high magnification). The figure also shows the worse interface bonding of monolithic Mg at very high tensile stresses. In contrast, delamination fracture in low magnification is not obvious for Mg/2 wt.%SiC_p, which is contributed to the relatively strong interface bonding; however, fracture surface in high magnification appears to have a brittleness character, which indicates a transgranular cleavage type failure mode.

Figure 13 and Table 2 present the results of microhardness measurements of Mg/2 wt.%SiC_p and monolithic Mg for various ARB cycles. Before the 6-ARB, there was no obvious difference between the microhardness values of two materials (in the range of 40~50 HV). However, from eighth ARB cycle, microhardness of Mg/2 wt.%SiC_p increases more greatly than monolithic Mg with cycles. Microhardness value of Mg/2 wt.%SiC_p reaches the maximum (~80.5 HV) at the fourteenth ARB cycle. For monolithic Mg, microhardness is not significantly improved with cycles. The higher microhardness for Mg/2 wt.%SiC_p (14-ARB) cycles as compared to monolithic Mg (14-ARB) and raw Mg may be attributed to (a) the presence of relatively harder ceramic particles in matrix [3]; (b) constraints on localized matrix deformation during indentation due to the presence of reinforcements; and (c) the reduced grain size (Table 1).

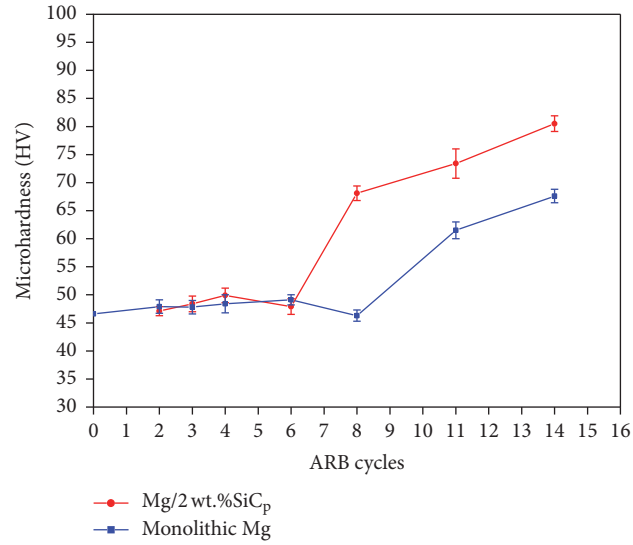

Figure 13: Microhardness of Mg/2 wt.%SiC_p and monolithic Mg produced by ARB process in various cycles.

4. Conclusions

In present work, Mg/2 wt.%SiC_p nanocomposite is successfully fabricated through ARB process. The microstructure and mechanical properties of nanocomposite were investigated. The homogeneous reinforcement distribution and superior mechanical properties were obtained after fourteen ARB cycles. The conclusions drawn from the results can be summarized as follows:

(1) By increasing the number of ARB cycles, a better distribution of SiC nanoparticles is obtained in magnesium matrix. The homogeneous distribution of nanoparticle in matrix is achieved after fourteen ARB cycles.

(2) After fourteen ARB cycles, a refined and uniform microstructure of Mg/2 wt.%SiC_p was obtained; the SiC nanoparticles contribute to grain refinement by stimulating the dynamic recrystallization (DRX) nucleation.

(3) A strong $\{0\ 0\ 0\ 2\}$ basal texture formed in both monolithic Mg and Mg/2 wt.%SiC_p during ARB process, and the addition of SiC nanoparticles could weaken the basal plane. After fourteen ARB cycles, Mg/2 wt.%SiC_p exhibited $(0\ 0\ 0\ 2)\ \langle 1\ 1\ -2\ 0\rangle$ recrystallization texture.

(4) After fourteen ARB cycles, nanocomposite exhibits much better mechanical properties than raw magnesium and monolithic magnesium. The UTS, YS, microhardness, and elastic modulus of nanocomposite are significantly increased by about 17.6%, 61%, 72.7%, and 80.8% compared to those of raw material, respectively.

Competing Interests

The authors declare that they have no competing interests.

References

[1] G. Cao, H. Konishi, and X. Li, "Mechanical properties and microstructure of SiC-reinforced Mg-(2,4)Al-1Si nanocomposites fabricated by ultrasonic cavitation based solidification processing," *Materials Science and Engineering: A*, vol. 486, no. 1-2, pp. 357–362, 2008.

[2] S. K. Thakur, "Microwave Synthesis and characterization of magnesium based composites containing nanosized SiC and hybrid ($SiC+Al_2O_3$) reinforcements," *Journal of Engineering Materials and Technology*, vol. 129, no. 2, pp. 194–199, 2006.

[3] M. Gupta, M. O. Lai, and D. Saravanaranganathan, "Synthesis, microstructure and properties characterization of disintegrated melt deposited Mg/SiC composites," *Journal of Materials Science*, vol. 35, no. 9, pp. 2155–2165, 2000.

[4] P. Poddar, V. C. Srivastava, P. K. De, and K. L. Sahoo, "Processing and mechanical properties of SiC reinforced cast magnesium matrix composites by stir casting process," *Materials Science and Engineering A*, vol. 460-461, pp. 357–364, 2007.

[5] H. Ferkel and B. L. Mordike, "Magnesium strengthened by SiC nanoparticles," *Materials Science and Engineering A*, vol. 298, no. 1-2, pp. 193–199, 2001.

[6] G. Cao, H. Choi, H. Konishi, S. Kou, R. Lakes, and X. Li, "Mg-6Zn/1.5%SiC nanocomposites fabricated by ultrasonic cavitation-based solidification processing," *Journal of Materials Science*, vol. 43, no. 16, pp. 5521–5526, 2008.

[7] K. B. Nie, X. J. Wang, X. S. Hu, L. Xu, K. Wu, and M. Y. Zheng, "Microstructure and mechanical properties of SiC nanoparticles reinforced magnesium matrix composites fabricated by ultrasonic vibration," *Materials Science and Engineering: A*, vol. 528, no. 15, pp. 5278–5282, 2011.

[8] T. S. Srivatsan, C. Godbole, M. Paramsothy, and M. Gupta, "Influence of nano-sized carbon nanotube reinforcements on tensile deformation, cyclic fatigue, and final fracture behavior of a magnesium alloy," *Journal of Materials Science*, vol. 47, no. 8, pp. 3621–3638, 2012.

[9] C. S. Goh, J. Wei, L. C. Lee, and M. Gupta, "Simultaneous enhancement in strength and ductility by reinforcing magnesium with carbon nanotubes," *Materials Science and Engineering: A*, vol. 423, no. 1-2, pp. 153–156, 2006.

[10] M. K. Habibi, M. Paramsothy, A. M. S. Hamouda, and M. Gupta, "Using integrated hybrid (Al+CNT) reinforcement to simultaneously enhance strength and ductility of magnesium," *Composites Science and Technology*, vol. 71, no. 5, pp. 734–741, 2011.

[11] C. W. Schmidt, C. Knieke, V. Maier, H. W. Höppel, W. Peukert, and M. Göken, "Accelerated grain refinement during accumulative roll bonding by nanoparticle reinforcement," *Scripta Materialia*, vol. 64, no. 3, pp. 245–248, 2011.

[12] M. Alizadeh and M. H. Paydar, "Fabrication of nanostructure Al/SiCP composite by accumulative roll-bonding (ARB) process," *Journal of Alloys and Compounds*, vol. 492, no. 1-2, pp. 231–235, 2010.

[13] R. Jamaati and M. R. Toroghinejad, "Manufacturing of high-strength aluminum/alumina composite by accumulative roll bonding," *Materials Science and Engineering: A*, vol. 527, no. 16-17, pp. 4146–4151, 2010.

[14] R. Jamaati and M. R. Toroghinejad, "High-strength and highly-uniform composite produced by anodizing and accumulative roll bonding processes," *Materials and Design*, vol. 31, no. 10, pp. 4816–4822, 2010.

[15] A. Yazdani and E. Salahinejad, "Evolution of reinforcement distribution in Al-B_4C composites during accumulative roll bonding," *Materials and Design*, vol. 32, no. 6, pp. 3137–3142, 2011.

[16] A. Yazdani, E. Salahinejad, J. Moradgholi, and M. Hosseini, "A new consideration on reinforcement distribution in the different planes of nanostructured metal matrix composite sheets prepared by accumulative roll bonding (ARB)," *Journal of Alloys and Compounds*, vol. 509, no. 39, pp. 9562–9564, 2011.

[17] C. Lu, K. Tieu, and D. Wexler, "Significant enhancement of bond strength in the accumulative roll bonding process using nanosized SiO_2 particles," *Journal of Materials Processing Technology*, vol. 209, no. 10, pp. 4830–4834, 2009.

[18] S. Salimi, H. Izadi, and A. P. Gerlich, "Fabrication of an aluminum-carbon nanotube metal matrix composite by accumulative roll-bonding," *Journal of Materials Science*, vol. 46, no. 2, pp. 409–415, 2011.

[19] S. J. Yoo, S. H. Han, and W. J. Kim, "Magnesium matrix composites fabricated by using accumulative roll bonding of magnesium sheets coated with carbon-nanotube-containing aluminum powders," *Scripta Materialia*, vol. 67, no. 2, pp. 129–132, 2012.

[20] L. R. Vaidyanath, M. G. Nicholas, and D. R. Milner, "Pressure welding by rolling," *British Welding Journal*, vol. 6, pp. 13–28, 1959.

[21] S. H. Lee, Y. Saito, N. Tsuji, H. Utsunomiya, and T. Sakai, "Role of shear strain in ultragrain refinement by accumulative roll-bonding (ARB) process," *Scripta Materialia*, vol. 46, no. 4, pp. 281–285, 2002.

[22] B. L. Li, N. Tsuji, and N. Kamikawa, "Microstructure homogeneity in various metallic materials heavily deformed by accumulative roll-bonding," *Materials Science and Engineering A*, vol. 423, no. 1-2, pp. 331–342, 2006.

[23] Y. Qiao, X. Wang, Z. Liu, and E. Wang, "Effect of temperature on microstructures, texture and mechanical properties of hot rolled pure Mg sheets," *Materials Science and Engineering: A*, vol. 568, pp. 202–205, 2013.

[24] Y. Saito, N. Tsuji, H. Utsunomiya, T. Sakai, and R. G. Hong, "Ultra-fine grained bulk aluminum produced by accumulative roll-bonding (ARB) process," *Scripta Materialia*, vol. 39, no. 9, pp. 1221–1227, 1998.

[25] N. Tsuji, Y. Ito, Y. Saito, and Y. Minamino, "Strength and ductility of ultrafine grained aluminum and iron produced by ARB and annealing," *Scripta Materialia*, vol. 47, no. 12, pp. 893–899, 2002.

[26] D. Lahiri, S. R. Bakshi, A. K. Keshri, Y. Liu, and A. Agarwal, "Dual strengthening mechanisms induced by carbon nanotubes in roll bonded aluminum composites," *Materials Science and Engineering: A*, vol. 523, no. 1-2, pp. 263–270, 2009.